Micro-motion extraction from spotlight SAR using a modified backprojection approach

Finlay Rollo[a], Christos Ilioudis[a], Greta Zefi[a], Alessandro Lotti[b], Daniel Tonelli[b], Massimo Zavagli[c], Mario Constantini[c], Daniele Zonta[b], Enrico Tubaldi[a], Pietro Millilo[d], Malcolm Macdonald[a], and Carmine Clemente[a]

[a]University of Strathclyde, Glasgow, UK
[b]University of Trento, Trento, Italy
[c]B-Open Solutions, Rome, Italy
[d]University of Houston, Houston, USA

ABSTRACT

Typically, an image formed using the backprojection algorithm is the coherent sum of every pulse's contribution to every image pixel, accounting for the respective time delays and phase corrections. This allows for highly accurate image reconstruction. The modification proposed, differs in that the contributions of every pulse are concatenated to form a 3D radar data cube, instead of being coherently summed. This approach allows for the precise analysis of how the phase of individual target pixels change over time. In this work, the phase is utilized to accurately reconstruct the amplitude and frequency of a vibrating target. This method is demonstrated on both simulated data and compensated phase history data (CPHD) acquired by Capella Space.

Keywords: micro-Doppler, micro-motion, vibration, SAR

1. INTRODUCTION

Synthetic Aperture Radar (SAR) is a radar technology designed to produce high-resolution imagery. By harnessing a moving platform, SAR effectively simulates a significantly larger antenna — an "aperture "— than physically possible. This dramatically increases the radar's resolution, enabling the creation of detailed images that would otherwise be unattainable with real aperture radar systems. One of the key advantages of SAR is its ability to capture images even under conditions of cloud cover, darkness, or adverse weather. As such, the applications of SAR are diverse and span several fields, including earth observation, military surveillance, disaster management, and environmental monitoring. This paper specifically explores the application of SAR in target characterization using the micro-Doppler effect.

When working with radar systems, a parameter of primary interest is the Doppler frequency. This is the shift in frequency between the transmitted and received radar pulse that corresponds to the relative, radial velocity between the target and the radar sensor. When the target - or components of the target - are undergoing small vibrations, rotations or oscillations, known in the literature as "micro-motions",[1] there is a corresponding modulation superimposed on the Doppler frequency. This is known as the micro-Doppler effect.[2] Some classic examples of the micro-Doppler effect are the rotating blades of a helicopter or the swinging arms and legs of a person walking.

Over the past 2 decades there has been significant interest in exploiting this phenomenon as an additional source of target information. This includes a very broad range of applications[3] with a particular focus on target recognition[4] due to the highly characterising nature of a target's unique micro-Doppler patterns - the so-called micro-Doppler signature. However, there is still a fairly limited carry over to SAR, with some notable works detailed in.[5–9] This is surprising given that the analysis and characterization of micro-motion effects have the potential to unlock a wealth of valuable information from SAR data. This information has far-reaching applications, including enhanced target classification[10] and structural health monitoring.[11]

Further author information: (Send correspondence to Finlay Rollo)
E-mail: finlay.rollo.2019@uni.strath.ac.uk

2. BACKPROJECTION ALGORITHM

SAR raw data must undergo significant processing to turn into useful information. At its core, SAR image formation is fundamentally a Fourier inversion problem with many algorithms having been developed for this. These are typically categorized into time domain or frequency domain approaches.

Frequency domain algorithms, such as the Polar Format Algorithm (PFA), are computationally efficient, with a complexity of $\mathcal{O}(N^2 \log N)$ for N pulses and an N×N image. In contrast, the backprojection algorithm (BPA) is notably more computationally intensive, with a complexity of $\mathcal{O}(N^3)$ for N pulses and an N×N image.[12] However, it offers significant advantages.

One of the key strengths of the BPA is its ability to easily accommodate motion compensation and non-linear trajectories on a pulse by pulse basis. It is also versatile and can be used in various SAR imaging modes, including stripmap, spotlight, and scan. Moreover, backprojection is well-suited for bistatic or multistatic SAR configurations, where each receiver may be positioned on a different slant range plane but the images can all be produced on the same reference grid.

The BPA does also have two mitigating features which help justify its use and ease its computational burden. For one, it is highly parallelizable, allowing for significantly faster processing when this is utilized. Secondly, it enables image formation to begin as soon as the first pulse is received, which can help offset the computational burden in particularly time-sensitive scenarios.

2.1 Standard Backprojection Algorithm

An image formed using the BPA is the coherent sum of every pulse's contribution to every image pixel. This allows for highly accurate image reconstruction with complete control over which pulses contribute to the final image, and what area of the scene is reconstructed.

Figure 1 shows a block diagram outlining the steps of the BPA.[13] The first step in the algorithm is the calculation of the differential range, requiring both the radar position at every pulse as well as the coordinates of every pixel on the predefined grid that the image is formed on. The differential range is defined as the difference between the distance between the radar and the current pixel and the radar and the scene centre point. This is expressed as in (1)[14]

$$\Delta R(\eta) = \sqrt{(x_a(\eta) - x)^2 + (y_a(\eta) - y)^2 + (z_a(\eta) - z)^2} - r_0(\eta) \tag{1}$$

where η represents slow time, $\Delta R(\eta)$ is the differential range, $x_a(\eta), y_a(\eta)$ and $z_a(\eta)$ are the positions of the radar antenna, x, y and z are the pixel locations and $r_0(\eta)$ is the range to scene centre.

The next step is the calculation of the phase correction and this is requires the differential range and the minimum frequency of every pulse and essentially implements an azimuth matched filter on a per pixel basis. The final step involves assigning a corresponding value to every pixel location for each received pulse, with the final image being formed by summation of these values. This process requires a linear interpolation step because the discretely sampled fast-time range bins do not necessarily align precisely with the distances between the radar and the pixels. The interpolation ensures that the pixel values accurately represent the reflected signal's strength at each location. Mathematically this is represented as in (2)[14]

$$I(\underline{r}) = \sum_{n=1}^{N_p} s_{\text{int}}(\underline{r}, \eta) \tag{2}$$

where $I(\underline{r})$ is the final image response for a pixel at location $\underline{r}$, N_p is the number of pulses and $s_{\text{int}}(\underline{r}, \eta)$ is the assigned pixel value.

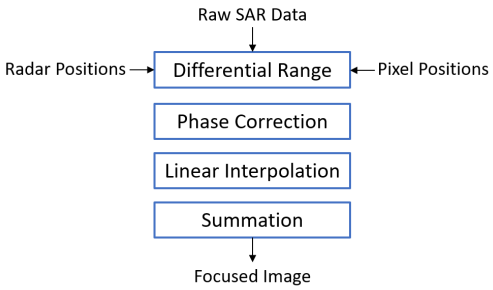

Figure 1: Block diagram of the standard BPA. Based on.[13]

2.2 Modified Backprojection Algorithm

Usually modifications are made to the BPA with the goal of speeding up the execution time[15,16] but they can also be used to include additional processing on an individual pulse basis, for example antenna gain compensation.[17] In this work, the core structure of the algorithm remains intact, with only the final summation step being changed. Here, it is replaced by a concatenation step, resulting in an output that forms a 3D data cube, with this new dimension representing the time axis. This results in a convenient way to track changes in the pixels over time. Of course, no meaningful image is created on the individual layers doing this, as the effective aperture is very small, but what is of interest is how the phase of the pixels change. By selecting an appropriate pixel of interest, such as one containing a vibrating target, details of the target's movement can be inferred from changes in the pixel's phase. These phase changes result from small movements that slightly alter the position of the target in the focused image.[6] It is this phase modulation that gives rise to the ghost artefacts or paired echoes effects seen in standard SAR focusing.

To visualise the different outputs of both algorithms Figure 2 shows a simplified version of an image produced by the standard BPA and as well as the data cube that is produced from the modified version. In both cases, a pixel of interest has been highlighted, with the array of pixel values from the data cube referred to as the signal of interest (SOI).

Utilizing the modified BPA to generate the SOI this way offers several advantages: (1) all micro-Doppler analysis techniques can be directly applied to the SOI without any additional preprocessing; (2) this method provides highly localized and precise micro-Doppler extraction in both time and space, making it particularly effective when dealing with closely spaced targets; (3) pulses can be coherently summed in smaller groups before concatenation, which enhances the signal-to-noise ratio (SNR) but lowers the effective pulse repetition frequency (PRF); (4) image formation is still possible by simply summing along the third dimension. The main limitation of processing SAR data in this fashion is the significant memory required to store the resulting data cube, although the computational time remains on par with the standard BPA.

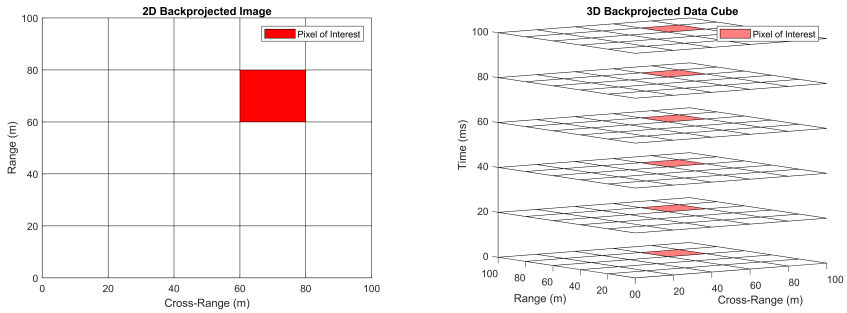

(a) (b)

Figure 2: a) Output of the standard BPA. b) Output of the modified BPA.

3. SIMULATED RESULTS

To first verify the proposed method, a simple SAR simulation was set up in MATLAB using ideal point targets. The simulation took parameters that could be found in a typical airborne, X-band SAR acquisition with a carrier frequency of 10 GHz, a pulse bandwidth of 200 MHz and a PRF of 400 Hz. The point target was set to have a vertical, sinusoidal vibration amplitude of 2 cm and a vibration frequency of 2 Hz. The SAR image from this simulation, formed using the standard BPA, is shown in Figure 3 where the paired echo effect can be seen clearly. The vibration of the target is centred around the centre of the scene.

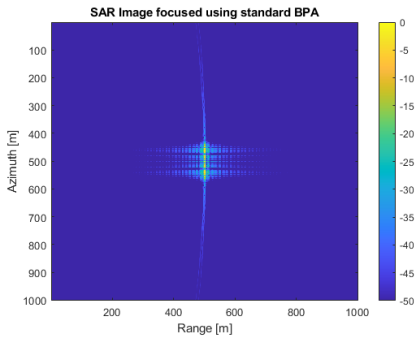

Figure 3: Simulated SAR Image focused using the standard BPA.

By running the modified BPA on the same raw data and selecting this central pixel as the pixel of interest, the targets movement can be analysed. This is done in two simple ways here, the first by applying a short-time Fourier transform (STFT) on the SOI. The STFT is expressed as in (3)

$$\chi(\nu, k) = \left| \sum_{n=0}^{N-1} s(n) w(n-k) e^{-j2\pi\nu n/N} \right|^2 \tag{3}$$

for a signal $s(n)$ as a function of n and total length N, a window function $w(n)$ of length k. The resulting spectrogram, with a window length of 25 samples, is shown in Figure 4 where the period of one oscillation is seen to be 0.5 s, corresponding to a frequency of 2 Hz, as expected. The Doppler frequency on the y-axis of the spectrogram corresponds to the velocity of the target but this is difficult to interpret visually here and so a more precise method is necessary. This can be achieved by analysing the phase of the SOI which can be related to distance by (4)

$$d = \frac{\Delta\phi \cdot \lambda}{4\pi} \tag{4}$$

where d is distance, $\Delta\phi$ is the phase difference between two points, and λ is the wavelength. By unwrapping the phase of the SOI and using the instantaneous phase in place of $\Delta\phi$ in (4), a time series of the line of sight displacement of the target within the pixel of interest can be reconstructed. This can be further refined by projecting the line of sight displacement into the vertical plane by (5)

$$d_{\text{vertical}} = \frac{d_{\text{LOS}}}{\sin(\gamma)} \tag{5}$$

where d_{vertical} is the vertical projection of displacement, d_{LOS} is the line of sight displacement, and γ is the grazing angle.

Both the line of sight and vertically projected displacements are shown in Figure 4 with the projected displacement perfectly matching the simulation ground truth of 2 cm. For targets with a complex vibration pattern, numerical differentiation could be used to determine the targets velocity as a function of time. Here however, with purely sinusoidal motion, a simple fast Fourier transform of the displacement time series is computed to calculate the frequency of vibration and it again it perfectly matches the ground truth of 2 Hz.

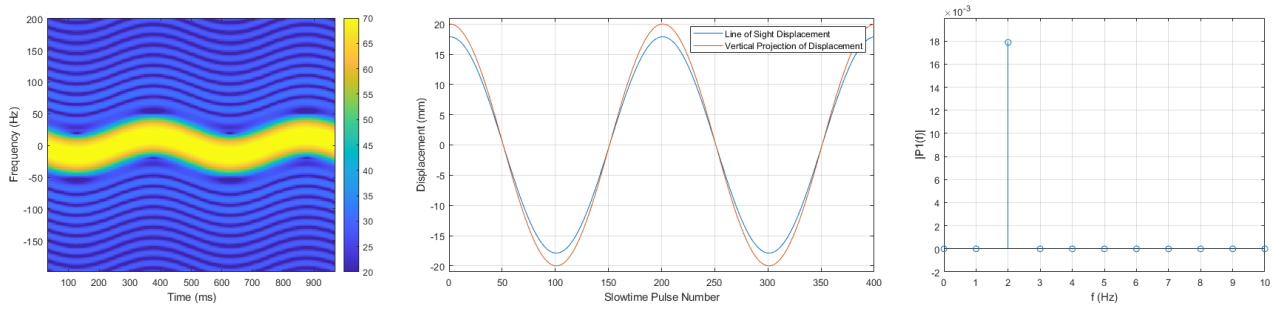

(a) (b) (c)

Figure 4: (a) Spectrogram of simulated SOI. (b) Reconstructed displacement of simulated target. (c) Frequency spectrum of simulated target displacement.

4. EXPERIMENTAL RESULTS

To further validate this approach, a SAR image was captured on 18$^{\text{th}}$ December 2023 over Trento, Italy, by Capella Space. During the acquisition an oscillating corner reflector was deployed as the ground truth, serving as the vibrating target. Specifically, the corner reflector was mounted on a programmable linear servo and a linear variable differential transformer (LVDT) sensor measured the reflector's precise displacement over time. The apparatus was positioned in an open field and was programmed for sinusoidal motion of 1.5 cm vertical vibration amplitude and 2 Hz vibration frequency during SAR acquisition. Figure 5 shows a section of the SAR image, with the location of the corner reflector highlighted, and the prominent paired echoes visible.

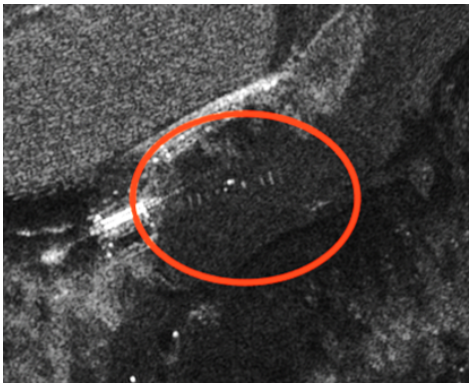

Figure 5: Section of SAR image with oscillating corner reflector circled. Image courtesy of Capella Space.

The modified BPA was run on the compensated phase history data (CPHD) of the acquisition and the SOI in this case was the central pixel of the paired echoes. To enhance the clarity of the spectrogram, the SOI was summed in batches of 100 - reducing the effective PRF from 10296 Hz to 102.96 Hz - and lowpass filtered. Figure 6 shows the resulting spectrogram and highlights another advantage of extracting the micro-motions in this way: the full length of the aperture can be used. The extended dwell from the Capella Space acquisition allows for almost 20 seconds of the corner reflectors motion to be observed.

The spectrogram is clearest at the start, likely due to the acquisition geometry and the orientation of the corner reflector producing the strongest returns. However, around 11, 15 and 16 seconds, the signal clarity diminishes, making it harder to extract useful information. Despite this, the vibration frequency can still be well estimated from the spectrogram. Approximately four oscillations occur within the first two seconds, indicating a vibration frequency of approximately 2 Hz. This aligns well with the ground truth, although it is challenging to draw definitive conclusions from visual inspection alone.

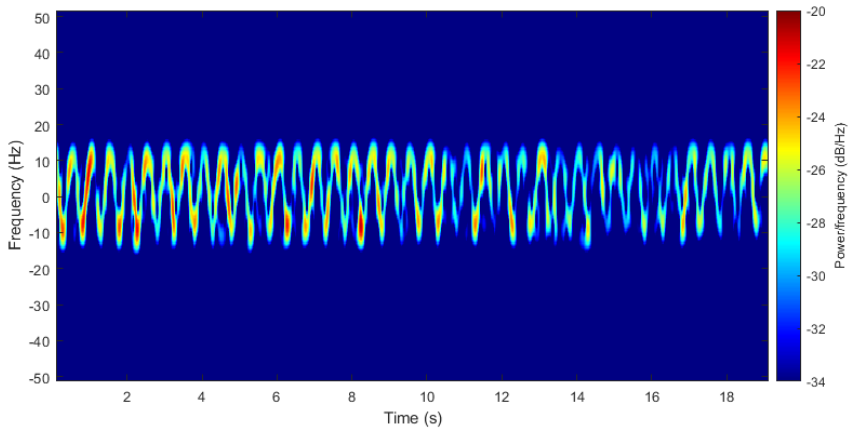

Figure 6: Spectrogram of experimental SOI.

Similar to the simulated results, the phase of the experimental SOI can be analyzed. By selecting samples from the first three seconds of the SOI and unwrapping the phase, the corresponding displacement can be calculated. Due to the accumulated errors in phase unwrapping, an additional step was necessary here: a linear detrend operation was performed using the least squares method. Utilizing equations (4) and (5), a vertical projection of the corner reflectors reconstructed displacement is shown in Figure 7. The projected displacement is plotted alongside the displacement measured by the LVDT. Initially, the timestamps from the SAR and the LVDT were used; however, the LVDT results were manually shifted by 0.1 seconds to achieve better alignment since the SAR and the ground truth were not synchronized.

The reconstructed displacement from the modified BPA aligns remarkably well with the ground truth data, achieving millimeter-level accuracy in certain areas. The alignment appears to be more precise at the valleys of the displacement rather than the peaks and this could be due to energy spill over from a neighbouring pixel that results in an over-estimate of the displacement. To verify the frequency, an FFT was performed on both the reconstructed displacement and the ground truth data, as shown in Figure 7. Both analyses exhibit a peak very close 2 Hz, with numerical values of 2.002 Hz for the ground truth and 2.01 Hz for the reconstructed frequency. Despite representing less than 3 seconds of data, this result underscores the effectiveness of this technique in reconstructing the displacement of a vibrating target.

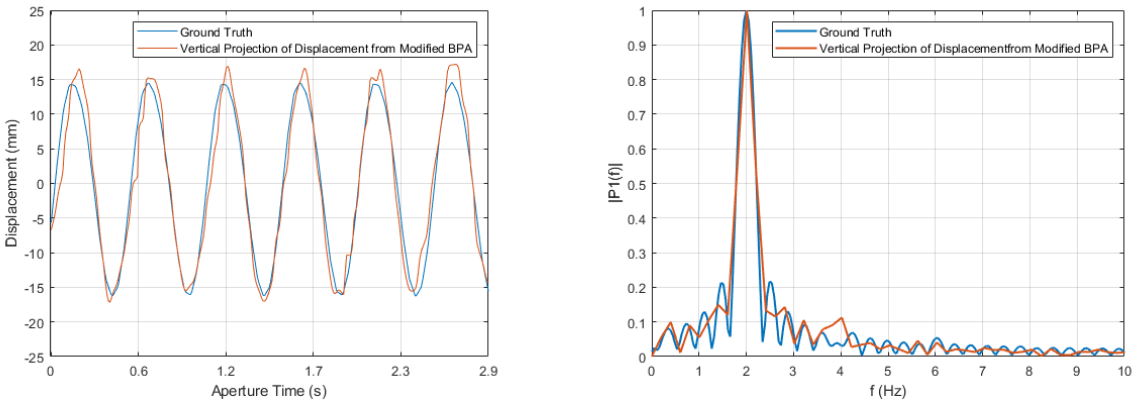

(a) (b)

Figure 7: (a) Reconstructed displacement of corner reflector. (b) Frequency spectra of displacement.

5. CONCLUSION

This work demonstrated a novel technique for extracting micro-Doppler information from SAR. By modifying the standard BPA and replacing the final summation step with a concatenation operation, a 3D data cube is formed with the new height axis representing time. By tracking the changes in phase of the cubes pixels through its layers (time), highly accurate target displacement and frequency can be reconstructed. The method was first tested on simulated MATLAB data and further verified on real, experimental data captured by Capella Space. Using the described approach the reconstructed displacement was found to be millimeter accurate in some places and the reconstructed frequency was 2.01 Hz against 2.002 Hz ground truth.

For future work, this method could be readily adapted to track a moving target by changing the pixel of interest across the layers, as there is no limitation requiring the selection of the same pixel throughout the entire process. Other methods could also be used to reconstruct the phase, such as the treating the micro-Doppler extraction as a polynomial phase signal estimation problem as in.[9]

ACKNOWLEDGMENTS

This research is funded by the European Space Agency under the projects "Bridge Monitoring Based on Single Pass SAR Images" and "EO4Security- Innovative SAR Processing Methodologies For Security Applications-Topic B2: MicroDoppler Processing".

This work was in part performed at the University of Houston under a contract with the NASA Commercial Smallsat Data Acquisition Program (QKWEF8XLMTT3).

Thanks to Capella Space for access to the datasets.

REFERENCES

[1] Chen, V., Li, F., Ho, S.-S., and Wechsler, H., "Micro-doppler effect in radar: phenomenon, model, and simulation study," *IEEE Transactions on Aerospace and Electronic Systems* **42**(1), 2–21 (2006).

[2] Chen, V., *The Micro-Doppler Effect in Radar, Second Edition*, ArchTech House (2019).

[3] Clemente, C., Balleri, A., Woodbridge, K., and Soraghan, J., "Developments in target micro-doppler signatures analysis: radar imaging, ultrasound and through-the-wall radar," *EURASIP J. Adv. Signal Process* , 47 (2013).

[4] Hanif, A., Muaz, M., Hasan, A., and Adeel, M., "Micro-doppler based target recognition with radars: A review," *IEEE Sensors Journal* **22**(4), 2948–2961 (2022).

[5] Ruegg, M., Meier, E., and Nuesch, D., "Vibration and rotation in millimeter-wave sar," *IEEE Transactions on Geoscience and Remote Sensing* **45**(2), 293–304 (2007).

[6] Sparr, T. and Krane, B., "Micro-doppler analysis of vibrating targets in sar," *IEE Proceedings - Radar, Sonar and Navigation* **150**, 277–283(6) (August 2003).

[7] Wang, Q., Pepin, M., Beach, R. J., Dunkel, R., Atwood, T., Santhanam, B., Gerstle, W., Doerry, A. W., and Hayat, M. M., "Sar-based vibration estimation using the discrete fractional fourier transform," *IEEE Transactions on Geoscience and Remote Sensing* **50**(10), 4145–4156 (2012).

[8] Wang, Y., Wang, Z., Zhao, B., and Xu, L., "Compensation for high-frequency vibration of platform in sar imaging based on adaptive chirplet decomposition," *IEEE Geoscience and Remote Sensing Letters* **13**(6), 792–795 (2016).

[9] Anghel, A., Vasile, G., Ioana, C., Cacoveanu, R., and Ciochina, S., "Micro-doppler reconstruction in spaceborne sar images using azimuth time–frequency tracking of the phase history," *IEEE Geoscience and Remote Sensing Letters* **13**(4), 604–608 (2016).

[10] Armenise, D., Biondi, F., Addabbo, P., Clemente, C., and Orlando, D., "Marine targets recognition through micro-motion estimation from sar data," in *2020 IEEE 7th International Workshop on Metrology for AeroSpace (MetroAeroSpace)*, 37–42 (2020).

[11] Biondi, F., Addabbo, P., Ullo, S. L., Clemente, C., and Orlando, D., "Perspectives on the structural health monitoring of bridges by synthetic aperture radar," *Remote Sensing* **12**(23) (2020).

[12] Mota, D., Cruz, H., Miranda, P. R., Duarte, R. P., de Sousa, J. T., Neto, H. C., and Véstias, M. P., "Onboard processing of synthetic aperture radar backprojection algorithm in fpga," *IEEE Journal of Selected Topics in Applied Earth Observations and Remote Sensing* **15**, 3600–3611 (2022).

[13] Cruz, H., Véstias, M., Monteiro, J., Neto, H., and Duarte, R. P., "A review of synthetic-aperture radar image formation algorithms and implementations: A computational perspective," *Remote Sensing* **14**(5) (2022).

[14] Gorham, L. A. and Moore, L. J., "SAR image formation toolbox for MATLAB," in *Algorithms for Synthetic Aperture Radar Imagery XVII*, Zelnio, E. G. and Garber, F. D., eds., **7699**, 769906, International Society for Optics and Photonics, SPIE (2010).

[15] Yegulalp, A., "Fast backprojection algorithm for synthetic aperture radar," in *Proceedings of the 1999 IEEE Radar Conference. Radar into the Next Millennium (Cat. No.99CH36249)*, 60–65 (1999).

[16] Ulander, L., Hellsten, H., and Stenstrom, G., "Synthetic-aperture radar processing using fast factorized back-projection," *IEEE Transactions on Aerospace and Electronic Systems* **39**(3), 760–776 (2003).

[17] Harrison, L. A. A., *Introduction to Synthetic Aperture Radar Using Python and MATLAB*, Archtech (2022).